

Orbital dichotomy of Fermi liquid properties in Sr_2RuO_4 revealed by Raman spectroscopy

Jean-Côme Philippe,^{1,*} Benoît Baptiste,² Chanchal Sow,³ Yoshiteru Maeno,³ Anne Forget,⁴ Dorothée Colson,⁴ Maximilien Cazayous,¹ Alain Sacuto,¹ and Yann Gallais^{1,†}

¹Université de Paris, Matériaux et Phénomènes Quantiques,

UMR CNRS 7162, Bâtiment Condorcet, 75205 Paris Cedex 13, France

²Sorbonne Université, Institut de Minéralogie, de Physique des Matériaux et de Cosmochimie,

UMR CNRS 7590, IMPMC, 4 place Jussieu, 75005 Paris, France

³Department of Physics, Kyoto University, Kyoto, Japan

⁴Service de Physique de l'Etat Condensé, DSM/DRECAM/SPEC, CEA Saclay, Gif-sur-Yvette, 91191, France

(Dated: May 20, 2022)

We report a polarization-resolved Raman spectroscopy study of the orbital dependence of the quasiparticles properties in the prototypical multi-band Fermi liquid Sr_2RuO_4 . We show that the quasiparticle scattering rate displays ω^2 dependence as expected for a Fermi liquid. Besides, we observe a clear polarization-dependence in the energy and temperature dependence of the quasiparticle scattering rate and mass, with the $d_{xz/yz}$ orbital derived quasiparticles showing significantly more robust Fermi liquid properties than the d_{xy} orbital derived ones. The observed orbital dichotomy of the quasiparticles is consistent with the picture of Sr_2RuO_4 as a Hund's metal. Our study establishes Raman scattering as a powerful probe of Fermi liquid properties in correlated metals.

Introduction

More than twenty-five years after the beginning of intensive research on Sr_2RuO_4 , following the discovery of its superconductivity [1], this material still exhibits a two-face status. On the one hand, despite numerous theoretical and experimental results, its superconducting state developing under 1.5 K remains a puzzle, with no definitive outcome about its parity and the gap structure [2, 3]. On the other hand, its normal state up to $T_{FL} \approx 25$ K is now described as the prototype of a quasi-two-dimensional Fermi liquid (FL) [4], so that "it is an established *unconventional* superconductor, with a *conventional* low-temperature normal state" [4].

The FL behavior is experimentally well established through the analysis of electron transport and optical conductivity measurements which display hallmarks of electron-electron interactions for a correlated FL state: the ω^2 and T^2 dependencies of scattering rate reflecting the low energy phase space constraints on electron-electron collisions. T^2 dependence of the in-plane DC resistivity is observed below $T_{FL} \sim 25$ K [5]. The corresponding ω^2 dependence of the scattering rate has been somewhat more elusive experimentally. Early Angle Resolved Photo-Emission Spectroscopy (ARPES) data indicated ω^2 dependence of the quasiparticle scattering rate, but the reported inverse lifetimes exceed the quasiparticle energies even at low energy, indicating they are likely not representative of the intrinsic bulk properties [6, 7]. Still, optical conductivity data show that in Sr_2RuO_4 the Gurzhi scaling law relating the T^2

and ω^2 prefactors of the scattering rate of a FL [8] is experimentally verified [9, 10]. Large effective masses m^* ranging from 3 to 5 times the band mass were measured via specific heat [11], quantum oscillations [4, 12], ARPES [13] and optical reflectivity measurements [9, 14, 15], which indicate significant electron correlations. Rather than the proximity to a Mott insulator, the Hund's rule coupling has been identified as the origin of heavy quasiparticle mass through Dynamical Mean Field Theory (DMFT) calculations [16, 17], labelling Sr_2RuO_4 as a Hund's metal.

The Fermi surface of this material is known in-depth from quantum oscillations [18, 19] and ARPES [13, 20]. It presents three quasi-cylindrical sheets α , β and γ : α and β come mainly from the hybridization of the one-dimensional d_{xz} and d_{yz} orbitals, whereas γ corresponds primarily to the two-dimensionnal d_{xy} orbital (Fig. 1). The multi-orbital nature of Sr_2RuO_4 induces some complications in the understanding of the experimental results since transport and optical conductivity measurements average the current response of the different Fermi sheets. Insight on the orbital dependent FL properties, a key feature of a Hund's metal, has been mostly limited to the static mass-enhancement factor which has been studied by quantum oscillations and ARPES measurements [13, 19]. Both indicate that the d_{xy} orbital derived quasiparticles are more correlated than the d_{xz} and d_{yz} ones, with larger static mass-enhancement, in agreement with DMFT calculations [16, 21]. Note that a similar orbital differentiation is also found in the magnetic sector, with possible implications for the still unsolved superconducting pairing mechanism of Sr_2RuO_4 [22, 23]: whereas antiferromagnetic fluctuations arise from the nested d_{xz} and d_{yz} derived bands, sub-leading ferromagnetic fluctuations are attributed to the d_{xy} derived band

*Electronic address: jeancome.philippe@u-paris.fr

†Electronic address: yann.gallais@u-paris.fr

[24, 25]. The coupling between the magnetic fluctuations is expected to lead to distinctive features in the orbital, wave-vector and energy dependence of the quasiparticle properties. A potential benchmark to test the respective influence of Hund’s rule coupling physics and low energy magnetic fluctuations can thus be reached by probing the orbital dependence of the quasiparticle dynamics in the FL state.

In this paper, we use polarization-resolved Raman spectroscopy to access the low energy quasiparticles dynamics of Sr_2RuO_4 in an orbital-resolved way. We show that the quasiparticle scattering rate displays ω^2 dependence as expected for a FL, thus mirroring the T^2 dependence observed in transport measurements. Besides, we observe a clear polarization-dependence in the energy and temperature dependence of the quasiparticle scattering rate and mass. We assign it to orbitally dependent FL properties with the d_{xy} derived quasiparticles being significantly more correlated than the d_{yz}/d_{xz} derived ones. The observed dichotomy is consistent with the picture of Sr_2RuO_4 as a Hund’s metal with significant orbital differentiation among quasiparticles. Our study establishes Raman scattering as a powerful probe of FL properties in multiband correlated metals.

Experiments

Raman experiments have been carried out using a triple grating JY-T64000 spectrometer in subtractive configuration with 1800 grooves/mm gratings. For measurements above 75 meV (discussed in the SM [26]), a single-stage configuration was used with 600 grooves/mm grating. When using the 1800 grooves/mm configuration, measurements could be performed down to 1 meV, with a resolution of 0.2 meV. The spectrometer is equipped with a nitrogen cooled CCD detector. We used the 532 nm excitation line from a diode pump solid state laser. Additional spectra (discussed in SM [26]) were obtained by using 488 nm and 660 nm wavelength lasers. Measurements between 3 and 200 K have been performed using a closed-cycle optical cryostat. Comparing temperature-dependent and laser-power-dependent spectra, we estimate laser heating to be $\Delta T \approx 4$ K (see SM for additional details [26]). All the raw spectra have been corrected for the Bose factor and the instrumental spectral response. They are thus proportional to the imaginary part of the Raman response function $\chi''(\omega, T)$.

As Sr_2RuO_4 belongs to the D_{4h} point group, the Raman-accessible symmetries are A_{1g} , E_g , B_{1g} and B_{2g} . For B_{2g} and B_{1g} symmetries measurements, the direction of incoming and outgoing electric fields are contained in the (ab) plane, with crossed polarizations along and at 45° from the Ru–O bond directions, respectively. For A_{1g} symmetry measurements presented here, the polarizations are parallel along the (c) axis (so we probe

the out-of-plane component of the A_{1g} channel). For E_g symmetry measurements, the direction of incoming electric field is along the (c) axis, the outgoing one is in the (ab) plane.

The single crystal of Sr_2RuO_4 used in our experiment was grown by the floating zone technique as described elsewhere [27]. Two different samples cut from the same single crystal were studied. One with an (ab) surface was used to access B_{2g} and B_{1g} symmetries, while the other with an (ac) surface was used to access $A_{1g}(c)$ and E_g symmetries. The crystallographic axes were determined via single-crystal X-ray diffraction prior to the Raman measurements.

Orbital dependence of Raman scattering symmetries in Sr_2RuO_4

The main conclusions of this work are based on the orbital selectivity of the B_{1g} and B_{2g} symmetries which we discuss first (more details can be found in the SM [26]). Within the effective mass approximation the amplitude of the Raman response, or Raman vertex, $\gamma^\mu(\mathbf{k})$ is symmetry dependent and given by the second derivatives of the band dispersion [28]. In orbital space ($a = xz/yz/xy$), the B_{1g} and B_{2g} Raman vertices corresponding to intra-orbital excitations are given by $\gamma_a^{B_{1g}}(\mathbf{k}) = \frac{1}{2}(\frac{\partial^2 \epsilon_a}{\partial k_x^2} - \frac{\partial^2 \epsilon_a}{\partial k_y^2})$ and $\gamma_a^{B_{2g}}(\mathbf{k}) = \frac{\partial^2 \epsilon_a}{\partial k_x \partial k_y}$. Using the hopping terms coming from the tight-binding model applicable to Sr_2RuO_4 [23, 29], with hopping integrals t_i , we obtain $\gamma_{xz/yz}^{B_{1g}}(\mathbf{k}) = t_{1/2} \cos(k_x) - t_{2/1} \cos(k_y)$, $\gamma_{xy}^{B_{1g}}(\mathbf{k}) = t_3(\cos(k_x) - \cos(k_y))$, $\gamma_{xz/yz}^{B_{2g}}(\mathbf{k}) = 0$ and $\gamma_{xy}^{B_{2g}}(\mathbf{k}) = 4t_4 \sin(k_x) \sin(k_y)$. Here the dominant hopping terms are t_1 the nearest neighbour Ru–Ru hopping between xz and yz orbitals along x and y respectively, and the nearest t_3 and next nearest t_4 neighbour Ru–Ru hopping between xy orbitals. The intra-orbital hoppings and the resulting Fermi surface are sketched in Fig. 1-(a-d). While the k dependent form factors are imposed by symmetry, the vanishing contribution of the d_{xz}/d_{yz} orbital in B_{2g} stems from the absence of next-nearest neighbour hopping between xz/yz orbitals. The orbital and k dependence of the vertices are sketched in Fig. 1-(e,f). In this simple picture, the B_{1g} channel probes intra-orbital excitations for both $d_{xz/yz}$ and d_{xy} orbitals with a priori similar weights ($t_1 \sim t_3$), providing limited orbital resolution. By contrast the B_{2g} channel only probes d_{xy} intra-orbital excitations, giving a unique access to the properties of the quasiparticles arising from this orbital. We note that inter-orbital excitations between d_{xz} and d_{yz} will also contribute to the B_{2g} channel, but with a weight about two orders of magnitude smaller than inter-orbital excitations due to the smallness of the inter-orbital hopping integrals [26].

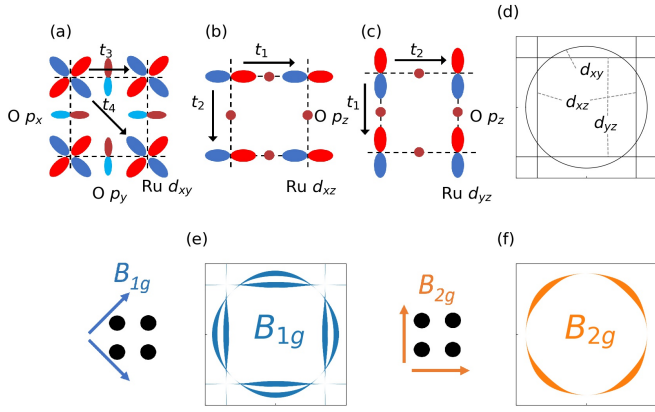


FIG. 1: (a,b,c) Schematic representation of the two-dimensional intra-orbital hopping integrals of the Ru d orbitals, t_i . (d) Schematic representation of the Fermi surface of Sr_2RuO_4 in the first Brillouin zone. (e,f) Sketch of the wave-vector dependence at the Fermi energy of the squared Raman vertex for intra-orbital transition terms in B_{1g} and B_{2g} channels. The local linewidth denotes the strength of the vertex. Note the nodes in the Raman vertex value along the diagonals or along the principal axis directions for B_{1g} and B_{2g} channels respectively. We took the values of t_i as $\{t_1, t_2, t_3, t_4\} = \{88, 9, 80, 40\}$ meV [29]. The sketches on the left of each vertex depict for each symmetry the polarizations of the incident and scattered beams with respect to the in-plane Ru square lattice.

Raman response of a Fermi liquid

Having discussed the orbital selectivity of Raman scattering, we now discuss the theoretically expected spectral lineshape of the Raman spectra of a FL which to our knowledge has not been discussed previously. We drop the temperature dependence for this discussion. In a simple Drude model the electronic Raman response reads [30, 31]:

$$\chi''_\mu(\omega) = \chi_\mu^0 \frac{\omega \Gamma_\mu}{\omega^2 + \Gamma_\mu^2} \quad (1)$$

with the index μ standing for the Raman symmetry channel, Γ_μ the symmetry resolved electronic scattering rate and χ_μ^0 the static susceptibility. In the Drude model, Γ_μ shows no energy dependence and can be assigned to static impurities. The Raman response displays a Drude peak at $\omega = \Gamma_\mu$ and then decreases with energy vanishing when $\omega \gg \Gamma_\mu$ (Fig. 2-(a)). For a FL with energy-dependent quasiparticle scattering rate $\Gamma_\mu(\omega)$ and mass-enhancement factor $1 + \lambda_\mu$, in close analogy with the current response of optical conductivity, the electronic Raman response can be modelled by the extended Drude model (EDM) (see also SM for a discussion of the validity of the EDM description for the Raman response [26]):

$$\chi''_\mu(\omega) = \tilde{\chi}_\mu^0 \frac{\omega \tilde{\Gamma}_\mu(\omega)}{\omega^2 + \tilde{\Gamma}_\mu(\omega)^2} \quad (2)$$

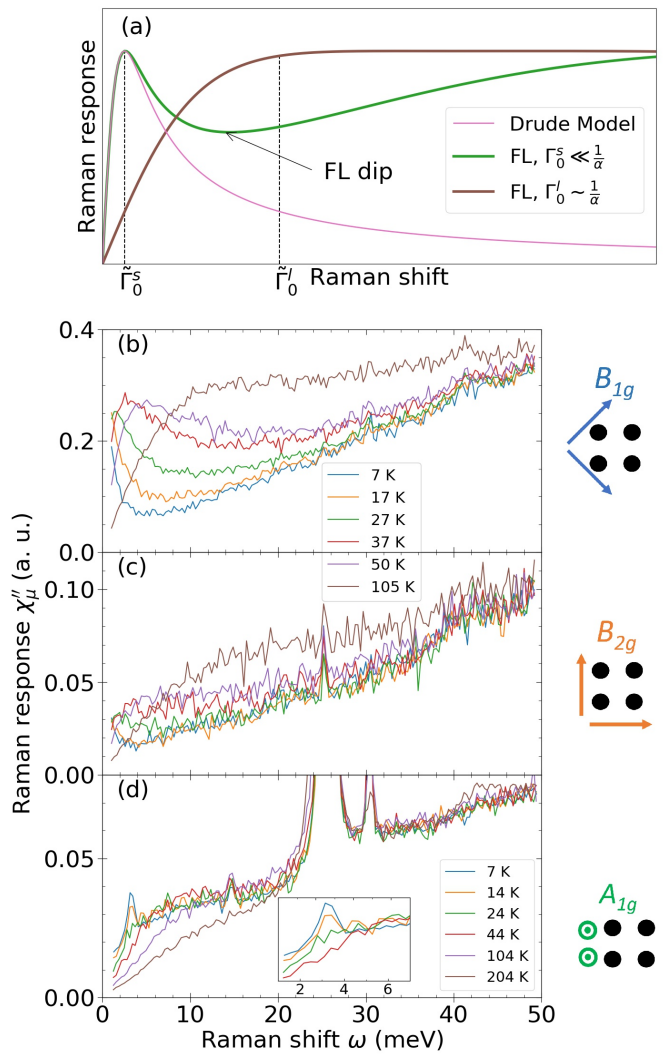


FIG. 2: (a) Theoretical Raman responses expected for a metal in the Drude model and for a FL in the extended Drude model. We took the small and the large $\tilde{\Gamma}_0$ as $\tilde{\Gamma}_0^l = 8\tilde{\Gamma}_0^s$. For the Drude model Γ_0 is taken equal to $\tilde{\Gamma}_0^s$. (b,c,d) Experimental Raman responses obtained in the B_{1g} , B_{2g} and A_{1g} symmetry channels at selected temperatures. The sketches on the right depict for each symmetry the polarizations of the incident and scattered beams with respect to the in-plane Ru square lattice. In the (d) panel, the inset shows the A_{1g} response below 7 meV.

where $\tilde{\chi}_\mu^0 = \frac{\chi_\mu^0}{1 + \lambda_\mu}$ and $\tilde{\Gamma}_\mu(\omega) = \frac{\Gamma_\mu(\omega)}{1 + \lambda_\mu}$. At low energy and below T_{FL} we expect $\Gamma_\mu(\omega) = \Gamma_{\mu,0} + \alpha_\mu \omega^2$ for the scattering and a constant mass-enhancement $1 + \lambda_\mu$. The main difference in the Raman response between Drude model and EDM is the non-monotonic lineshape of the response beyond the Drude peak, leading to a characteristic FL "dip" in the Raman spectra separating the Drude regime at lower energy, and the thermal regime at higher energy in close analogy with the FL "foot" of optical conductivity [32]. Increasing the static $\Gamma_{\mu,0}$ by increasing temperature and/or disorder, the Drude peak

hardens, causing the FL dip to resorb and making the Raman response more Drude-like. The disappearance of the FL dip occurs when $\Gamma_{\mu,0} \sim \frac{1}{\alpha}$. The presence of the FL dip in the Raman spectrum is a clear fingerprint of FL behavior, which to our knowledge has not been reported up to now. Instead, the flat Raman continua observed in correlated metals like cuprates [33], and iridates [34] have been interpreted as signaling non-FL "marginal" like behavior, with a quasiparticle scattering rate following linear rather than quadratic energy dependence. From this perspective Sr_2RuO_4 provides an interesting model system to establish canonical FL behavior in the Raman scattering spectrum.

Results

The spectra obtained in B_{1g} , B_{2g} and A_{1g} symmetries are depicted in Fig. 2-(b,c,d) at selected temperatures (more temperatures for B_{1g} and B_{2g} can be found in the SM [26]). As discussed previously, ab plane-polarized B_{1g} and B_{2g} symmetries probe in-plane quasiparticle excitations arising from d_{xz} , d_{yz} and d_{xy} orbitals. On the other hand the c -axis polarized A_{1g} symmetry probes out-of-plane quasiparticle excitations related to the weak interlayer hopping process. The spectra obtained in mixed E_g symmetry are shown in the SM [26]. In B_{1g} and B_{2g} symmetries, the spectra are dominated by the electronic continuum and are essentially free from any phononic contribution, as expected for the I4/mmm space group of Sr_2RuO_4 . Besides the continuum, the A_{1g} spectra also display narrow peaks assigned to the A_{1g} optical phonon modes coming from c -axis motion of Sr atoms, and a leakage from the E_g phonon coming from ab plane motion of Sr atoms respectively [35–37].

In all symmetries the signal remains unchanged up to at least 200 K above around 50 meV, but we observe a significant temperature dependence of the low energy response. In B_{1g} symmetry the shape of the Raman spectrum below 100 K is consistent with the response expected for a FL described above. It contains both a low energy Drude peak and a FL dip at higher energy. The Drude peak hardens and broadens and the FL dip resorbs as temperature increases, in qualitative agreement with a static relaxation rate $\Gamma_{B_{1g},0}$ increasing with temperature. In B_{2g} the temperature evolution is qualitatively similar, but with key differences: the Drude peak is strongly reduced with respect to the continuum at higher energy. A weaker FL dip can still be resolved but below 50 K instead of 85 K at least in the B_{1g} channel (see also spectra at higher temperatures in SM [26]). Below 10 K and in both symmetries, the Drude peak maximum shifts well below our low energy cutoff at 1 meV, indicating an extremely low residual scattering rate due to disorder.

The A_{1g} response is qualitatively different from the in-plane symmetries, with an almost flat continuum in the whole spectral range. Above 20 K no clear FL dip is resolved and a much broader Drude peak is observed,

indicating a significantly larger static relaxation rate in this out-of-plane channel, consistent with transport measurements [38]. Below 20 K, a narrow peak develops around 3.5 meV. This peak is too sharp and symmetric to be assigned to a Drude-like response, or an interband transition. Instead, we tentatively assign a collective excitation, possibly a c -axis plasmon, which would correspond to the onset of coherent c -axis transport observed in resistivity measurements below $\sim T_{FL}$ [38]. We note that recent momentum-resolved electron energy loss spectroscopy (M-EELS) measurements in Sr_2RuO_4 report a dispersive collective mode of electronic origin. The $q = 0$ intercept of the M-EELS mode falls below 10 meV, and could therefore correspond to the same excitation as the one observed in our c -axis A_{1g} Raman spectrum [39].

In the following we will focus on the FL analysis of the in-plane quasiparticle dynamics obtained from B_{1g} and B_{2g} symmetry spectra.

Analysis of the symmetry-resolved Fermi liquid properties

From the B_{1g} and B_{2g} Raman spectra we can extract the symmetry resolved relaxation rate Γ_μ and mass-enhancement factor $1 + \lambda_\mu$ using the extended Drude model (Eq. 2), or equivalently the memory-function approach [33, 40]. This method, widely used for the analysis of the optical conductivity spectrum of correlated electron systems, was first introduced by Opel et al. [33] to analyze the normal state Raman response of high- T_c cuprates. It is described in details in the SM [26]. For a FL, the relaxation rate is expected to follow a quadratic behavior both in energy and temperature, below some crossover temperature T_{FL} and energy ω_{FL} .

$$\Gamma_\mu(\omega, T) = \Gamma_{\mu,00} + \alpha_\mu \omega^2 + \beta_\mu (k_B T)^2 \quad (3)$$

First we consider the energy dependence of Γ_μ and $1 + \lambda_\mu$ at 15 K, deep in the FL transport regime (Fig. 3). As shown in Fig. 3-(a,b), there is a significant symmetry dependence of both quantities with $\Gamma_{B_{1g}} < \Gamma_{B_{2g}}$ and $1 + \lambda_{B_{1g}} < 1 + \lambda_{B_{2g}}$ over the whole relevant energy range. Also, the scattering rate follows ω^2 behavior over a significantly broader energy range in B_{1g} symmetry compared to B_{2g} symmetry. We estimated the range of $\omega_{FL,\mu}$ by performing quadratic fits of low energy $\Gamma_\mu(\omega)$ and tracking the energy at which a departure from quadratic behavior is resolved (see SM [26] for further details). Considering all probed temperatures below 40 K, we obtain $\omega_{FL,B_{1g}} \sim 15 - 20$ meV and $\omega_{FL,B_{2g}} \sim 8 - 12$ meV, with a clear quantitative dichotomy between the two channels.

From the quadratic fits we obtain the ω^2 FL coefficient α_μ in both symmetries. As shown in Fig. 3-(c) α_μ shows a weak temperature dependence in both symmetries, and despite larger uncertainties in B_{2g} symmetry, $\alpha_{B_{2g}} >$

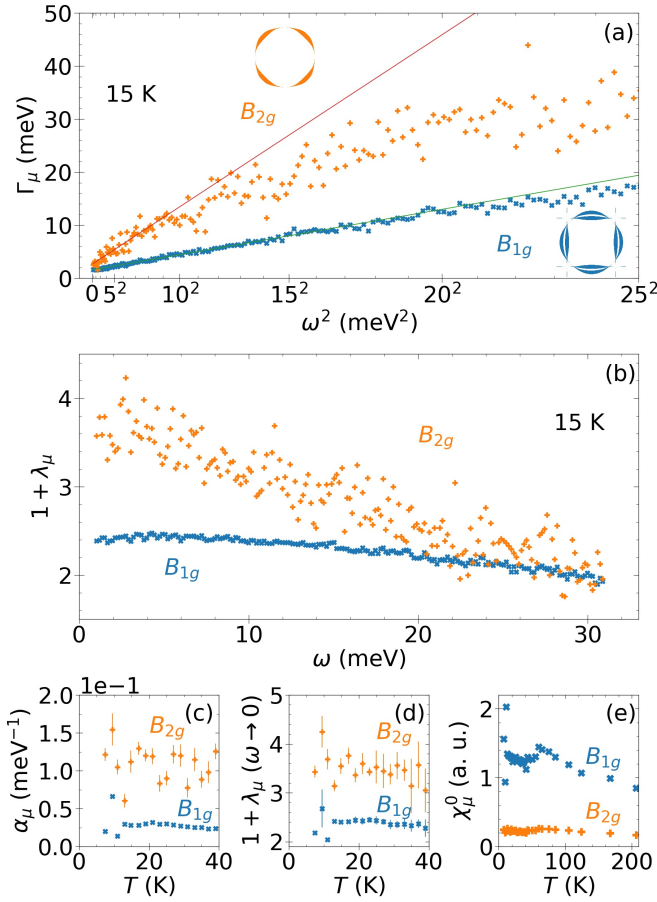


FIG. 3: (a) Energy dependence of the relaxation rate $\Gamma_\mu(\omega)$ at 15 K for B_{1g} and B_{2g} . The solid lines are quadratic fits of the experimental data at low energy. The sketches remind the shape of the Raman vertices (see Fig. 1). (b) Low energy dependence of the mass-enhancement factor $1 + \lambda_\mu$ at 15 K in B_{1g} and B_{2g} . (c) Temperature dependence of the ω^2 prefactor of $\Gamma_\mu(\omega)$, obtained through the fits. The error bars are computed as statistical uncertainty in the quadratic fits. (d) Temperature dependence of the extrapolated zero-energy mass-enhancement. (e) Temperature dependence of the Raman static susceptibility.

$\alpha_{B_{1g}}$ holds in the entire temperature range. The greater dispersion below 12 K is linked with the fact that in this temperature range the Drude peak is below the low energy experimental Raman cut-off. This causes difficulties in accurately extrapolating the experimental data to zero energy, and so a greater uncertainty in all the extracted quantities (see SM for further details on the spectra low energy extrapolation [26]). To estimate quantitative values of α_μ deep in the FL state, we consider values between 12 and 25 K. Overall, taking the average of the values in this temperature range we obtain $\alpha_{B_{2g}} \approx 3\alpha_{B_{1g}}$.

The mass-enhancement factor decreases with energy in both symmetries and stays larger than unity at high energy. It is flatter at low energy in B_{1g} symmetry as expected for a FL where it should be constant below ω_{FL}

[32], and in agreement with the more robust FL behavior observed in the scattering rate in the same symmetry. The extrapolated values at low energy $1 + \lambda_\mu(\omega \rightarrow 0)$ are weakly temperature dependant below 40 K but display a significant symmetry dependence, with $1 + \lambda_0^{B_{2g}} \approx 1.5(1 + \lambda_0^{B_{1g}})$, and values ranging from 2.5 to 4 (Fig. 3-(d)).

Finally the symmetry-resolved static susceptibility χ_μ^0 (Fig. 3-(e)) displays a mild dependence on temperature with a gradual increase in both symmetry channels upon cooling from 200 K to 60 K, followed by an essentially flat temperature dependence below 60 K. This indicates the absence of any significant symmetry breaking nematic-like instability in the B_{1g} or B_{2g} channels.

Focusing now on the temperature dependence of the scattering rate, we define the static relaxation rate $\Gamma_{\mu,0}(T)$ as the extrapolated relaxation rate at zero energy obtained through the quadratic energy fits. Its temperature dependence is depicted in figure 4 - (a). We fit the $\Gamma_{\mu,0}(T)$ data below 27 K by a quadratic behavior and we estimate $T_{FL,\mu}$ as the range above which the data visually deviate from the fit. We define $\Gamma_{\mu,00}$ as the zero temperature value of the fitted $\Gamma_{\mu,0}(T)$. We have significantly less experimental points in temperature than in energy, so it is more difficult to estimate the range of $T_{FL,\mu}$. We estimate $T_{FL,B_{1g},B_{2g}} \approx 20 - 30$ K, and we can extract the symmetry resolved T^2 prefactor β_μ . We cannot conclude about a dichotomy between $T_{FL,B_{1g}}$ and $T_{FL,B_{2g}}$, but, despite larger uncertainties compared to ω^2 coefficient, it is clear that $\beta_{B_{2g}} > \beta_{B_{1g}}$.

The Table I summarizes the FL parameters in both symmetry channels. The different values of α_μ , β_μ , $\omega_{FL,\mu}$ and $1 + \lambda_\mu(\omega \rightarrow 0)$ suggest that the FL state is more robust in the B_{1g} than in the B_{2g} channel: the quasiparticles probed via B_{2g} are more correlated than the ones probed via B_{1g} . Given the orbital dependence of each symmetry channel discussed previously, we can conclude that the electrons originating from the d_{xy} orbital are significantly more correlated than the ones derived from the $d_{xz/yz}$ orbitals.

Discussion

The orbital differentiation in the FL properties of Sr_2RuO_4 is consistent with previous experimental and theoretical results highlighting the more correlated status of the γ band arising from the d_{xy} orbital. This orbital differentiation has been mostly documented via the mass-enhancement factor through de Haas van Alphen (dHvA), and more recently ARPES measurements [13]. The dHvA oscillations results give the zero energy and low temperature thermodynamic cyclotron masses in each band at the Fermi level, measuring enhancement of 3.0, 3.5 and 5.5 with respect to the band masses (taken from [41]) respectively for the $d_{xz/yz}$ and d_{xy} derived Fermi sheets. Similar values are found by ARPES [13]. Our mass-enhancement values are somewhat lower, but

| | ω_{FL} (meV) | α (10 ⁻² meV ⁻¹) | β (10 ⁻¹ meV ⁻¹) | Γ_{00} (meV) | p | $1 + \lambda_\mu(\omega \rightarrow 0)$ |
|----------|---------------------|--|---|---------------------|----------------|---|
| B_{1g} | 15 – 20 | 3.0 ± 0.2 | 6.9 ± 0.2 | 0.45 ± 0.06 | 1.6 ± 0.1 | 2.45 ± 0.05 |
| B_{2g} | 8 – 12 | 10 ± 3 | 8.9 ± 0.2 | 1.16 ± 0.05 | 0.85 ± 0.1 | 3.5 ± 0.5 |

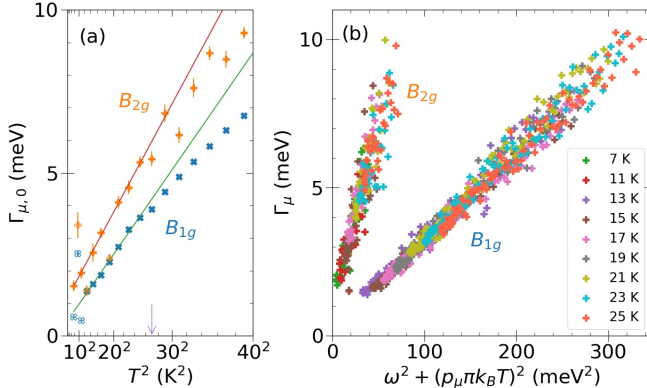
TABLE I: FL parameters differentiation in B_{1g} and B_{2g} channels.

FIG. 4: (a) Temperature dependence of the extrapolated static relaxation rate $\Gamma_{0,\mu}$ for B_{1g} and B_{2g} . The solid lines are quadratic fits of the low temperature data. The arrow denotes the upper limits of the fits at 27 K. The empty symbols are excluded for the computation of the fits. (b) Gurzhi scaling law with $p_{B_{1g}} = 1.6$ and $p_{B_{2g}} = 0.85$.

this might be attributed to the cut-off parameter ω_c used to extract the Raman-derived quasiparticle properties which has a logarithmic influence on Γ and $1 + \lambda$ making our values likely underestimated [26]. Still, the ratio of mass-enhancement between both Raman symmetries, 1.5, is close to the one between d_{xy} and $d_{xz/yz}$ orbital derived Fermi sheets found in quantum oscillation measurements, and also in DMFT calculations [16]. From this, we can conclude that the B_{1g} FL parameters are likely dominated by quasiparticles coming from $d_{xz/yz}$ orbitals. This is not completely intuitive since as stressed in the discussion of Raman vertices, we expect this symmetry to have roughly equal contributions from each orbitals. More realistic calculations of the Raman responses, including spin-orbit coupling and the full Fermi surface topology [13, 42], are needed to further assess this point.

Besides the mass enhancement, an interesting feature of our Raman results is the ability to simultaneously track the energy and temperature behaviors of the scattering rate. The link between these quantities and the mass enhancement has traditionally been discussed in terms of the Kadowaki-Woods (KW) ratio which links the mass enhancement as measured by the Sommerfeld coefficient of the electronic specific heat and the T^2 coefficient of resistivity measurements [43, 44]. This ratio has been shown to be approximately constant within different class of materials like transition metals [43] and 4f-electron heavy fermions systems [44], indicating

that it is relatively immune to the strength of electron correlations. However, the ratio is also known to depend sensitively on band structure details such as dimensionality, band-width and Fermi velocities [45, 46]. An additional source of complication in multiband systems with sizeable Hund's rule coupling is the impact of orbital differentiation on the KW ratio. Indeed transport measurements are dominated by high velocity bands, while specific heat is dominated by d_{xy} derived γ sheets. Insight into this orbital dependence can be obtained by computing similar ratios for both symmetries using the extracted mass-enhancement and the ω^2 or T^2 coefficient of the scattering rate. These ratios display sizeable symmetry dependence $(\frac{\alpha}{(1+\lambda)^2})_{B_{1g}/B_{2g}} \sim 5/8$ eV⁻¹ and $(\frac{\beta}{(1+\lambda)^2})_{B_{1g}/B_{2g}} \sim 115/72$ eV⁻¹ pointing to an orbital dependence of such ratio within the same material. We note that a strong variation of the KW ratio was recently found in Sr_2RuO_4 under uni-axial strain. It was attributed to the proximity of the d_{xy} derived γ sheet to a van Hove singularity in the density of state [47]. These findings confirm the strong sensitivity of such ratios to material specific band structure details such as orbital content and density of states.

Another hallmark of FL behavior is the scaling between the T^2 and ω^2 coefficients. For a FL α_μ and β_μ are related through the Gurzhi scaling law [8, 48]:

$$\frac{\beta_\mu}{\alpha_\mu} = (p_\mu \pi)^2, \quad (4)$$

For two-particle probes like optical conductivity and Raman spectroscopy one expects $p = 2$. In practice the few materials where the scaling has been studied via optical conductivity have yielded p values significantly different from 2 [10, 49–53]. Deviations from the Gurzhi scaling have been attributed to energy dependent elastic scattering effects which contribute to an energy but not a temperature dependence in the quasiparticle self-energy [10]. A notable exception is Sr_2RuO_4 where Stricker et al. have reported a value very close to 2, albeit at temperatures, 30–40 K, slightly above T_{FL} [9]. We have attempted a similar scaling with our data by plotting Γ_μ as a function of $\omega^2 + (p_\mu \pi k_B T)^2$ and taking p as a symmetry dependent free parameter (Fig. 4-(b) and SM [26]). The best scaling are obtained using respectively $p \approx 1.6$ and $p \approx 0.85$ in B_{1g} and B_{2g} , with greater uncertainties in B_{2g} , but indicating $p < 2$ for both symmetries. Since no systematic temperature dependence is found for p between 10 and 40 K, the discrepancy between Raman spectroscopy and optical conductivity cannot be simply attributed

to the temperature of the measurements with respect to the FL coherence temperature T_{FL} . Both the symmetry dependence and the discrepancy between Raman spectroscopy and optical conductivity lead us to speculate that elastic scattering effects on quasiparticle scattering rate might be orbital dependent.

Overall, the symmetry dependence of the quasiparticles dynamics as probed by Raman scattering are consistent with the picture of a Hund's metal, with robust FL properties for $d_{xz/yz}$ -derived quasiparticles, but more fragile for d_{xy} -derived ones. A remaining issue is the role of magnetic fluctuations in the strong symmetry dependence of the Raman spectra. Up to now we have essentially ignored the additional k dependence embedded in the Raman vertices with the B_{1g} and B_{2g} vertex having line nodes at 45° and along the principal axes respectively. In particular incommensurate antiferromagnetic fluctuations are expected to impact mostly the $d_{xz/yz}$ derived quasiparticles with hot spots located at their crossing. It is interesting to note that the B_{1g} vertex precisely vanishes at these points and the B_{2g} vertex has no amplitude on these orbitals. Besides, the energy dependent scattering rates suggest a gradual departure from FL behavior with a characteristic symmetry dependent crossover energy ω_{FL} , without any sharp kink that could be attributed to the coupling to magnetic fluctuations (ferromagnetic and antiferromagnetic) whose characteristic energy scales lie in the energy windows studied here, below 20 meV [25]. Therefore, it appears magnetic fluctuations may not play a prominent a role in the dichotomy observed in the Raman spectra.

In conclusion, we have shown that Sr_2RuO_4 provides an attractive model system to demonstrate the ability of Raman scattering to probe orbital dependent FL properties. Our results can serve as a standard for future Raman studies aiming at probing exotic physics such as non-FL and quantum criticality. The strong dichotomy observed is in-line with the picture of Sr_2RuO_4 as a Hund's metal with coexisting robust and fragile quasiparticles. A comparison with realistic calculations

of the symmetry resolved Raman spectra using for e.g. DMFT techniques should provide a more quantitative test of the Hund's metal picture. Finally, whether the observed orbital dichotomy plays a role in the superconducting pairing is an intriguing issue in light of the recent proposals of an orbital anti-symmetric chiral pairing state which was argued to reconcile several key experimental observations [54, 55].

Competing interests

The authors declare they have no competing interests

Acknowledgments

The authors acknowledge insightful discussions with Antoine Georges, Dimitri Maslov, Indranil Paul and Yvan Sidis

Data sharing

All relevant data are included in the main manuscript and the supplementary materials.

Author Contributions

Y. G. designed research. J.-C. P., B. B., A. F., D. C., C. S., Y. M., M. C., A. S. and Y. G. performed research. J. -C. P. and Y. G. analyzed data. J. -C. P. and Y. G. wrote the paper.

Funding

J.-C. P., M. C., A. S. and Y. G. acknowledge the support from ANR Grant NEPTUN (ANR-19-CE30-0019-03)

[1] Y. Maeno, H. Hashimoto, K. Yoshida, S. Nishizaki, T. Fujita, J. G. Bednorz, and F. Lichtenberg, *Nature* **375**, 532 (1994).

[2] A. P. Mackenzie, T. Scaffidi, C. W. Hicks, and Y. Maeno, *npj Quantum Materials* **2**, 40 (2017), ISSN 2397-4648, URL <http://www.nature.com/articles/s41535-017-0045-4>.

[3] A. Pustogow, Y. Luo, A. Chronister, Y.-S. Su, D. A. Sokolov, F. Jerzembeck, A. P. Mackenzie, C. W. Hicks, N. Kikugawa, S. Raghu, et al., *Nature* **574**, 72 (2019), ISSN 1476-4687, URL <https://www.nature.com/articles/s41586-019-1596-2>.

[4] C. Bergemann, A. P. Mackenzie, S. R. Julian, D. Forsythe, and E. Ohmichi, *Advances in Physics* **52**, 639 (2003), ISSN 0001-8732, 1460-6976, URL <http://www.tandfonline.com/doi/abs/10.1080/00018730310001621737>.

[5] Y. Maeno, S. Nishizaki, K. Yoshida, S.-i. Ikeda, and T. Fujita, *Journal of Low Temperature Physics* **105**, 1577 (1996).

[6] N. J. C. Ingle, K. M. Shen, F. Baumberger, W. Meevasana, D. H. Lu, Z.-X. Shen, A. Damascelli, S. Nakatsuji, Z. Q. Mao, Y. Maeno, et al., *Physical Review B* **72**, 205114 (2005), ISSN 1098-0121, 1550-235X, URL <https://link.aps.org/doi/10.1103/PhysRevB.72.205114>.

[7] T. E. Kidd, T. Valla, A. V. Fedorov, P. D. Johnson, R. J. Cava, and M. K. Haas, *Physical Review Letters* **94**, 107003 (2005), ISSN 0031-9007, 1079-7114, URL <https://link.aps.org/doi/10.1103>

PhysRevLett. **94**, 107003.

[8] R. N. Gurzhi, Soviet Physics Journal of Experimental and Theoretical Physics **35** (8), 673 (1959).

[9] D. Stricker, J. Mravlje, C. Berthod, R. Fittipaldi, A. Vecchione, A. Georges, and D. van der Marel, Physical Review Letters **113**, 087404 (2014).

[10] D. L. Maslov and A. V. Chubukov, Reports on Progress in Physics **80**, 026503 (2017), ISSN 0034-4885, 1361-6633, URL <https://iopscience.iop.org/article/10.1088/1361-6633/80/2/026503>.

[11] Y. Maeno, K. Yoshida, H. Hashimoto, S. Nishizaki, S.-i. Ikeda, M. Nohara, T. Fujita, A. P. Mackenzie, N. E. Hussey, J. G. Bednorz, et al., Journal of the Physical Society of Japan **66**, 1405 (1997).

[12] A. Mackenzie, S.-i. Ikeda, Y. Maeno, T. Fujita, S. Julian, and G. Lonzarich, Journal of the Physical Society of Japan **67**, 385 (1998), ISSN 0031-9015, 1347-4073, URL <http://journals.jps.jp/doi/10.1143/JPSJ.67.385>.

[13] A. Tamai, M. Zingl, E. Rozbicki, E. Cappelli, S. Ricco, A. de la Torre, S. McKeown Walker, F. Y. Bruno, P. D. C. King, W. Meevasana, et al., Physical Review X **9**, 021048 (2019).

[14] T. Katsufuji, M. Kasai, and Y. Tokura, Physical Review Letters **76**, 126 (1996).

[15] J. S. Lee, S. J. Moon, T. W. Noh, S. Nakatsuji, and Y. Maeno, Physical Review Letters **96**, 057401 (2006), ISSN 0031-9007, 1079-7114, URL <https://link.aps.org/doi/10.1103/PhysRevLett.96.057401>.

[16] J. Mravlje, M. Aichhorn, T. Miyake, K. Haule, G. Kotliar, and A. Georges, Physical Review Letters **106**, 096401 (2011).

[17] A. Georges, L. d. Medici, and J. Mravlje, Annual Review of Condensed Matter Physics **4**, 137 (2013), ISSN 1947-5454, 1947-5462, URL <http://www.annualreviews.org/doi/10.1146/annurev-conmatphys-020911-125045>.

[18] A. P. Mackenzie, S. R. Julian, A. J. Diver, G. J. McMullan, M. P. Ray, G. G. Lonzarich, Y. Maeno, S. Nishizaki, and T. Fujita, Physical Review Letters **76**, 3786 (1996).

[19] C. Bergemann, S. R. Julian, A. P. Mackenzie, S. Nishizaki, and Y. Maeno, Physical Review Letters **84**, 2662 (2000).

[20] A. Damascelli, D. H. Lu, K. M. Shen, N. P. Armitage, F. Ronning, D. L. Feng, C. Kim, Z.-X. Shen, T. Kimura, Y. Tokura, et al., Physical Review Letters **85**, 5194 (2000).

[21] F. B. Kugler, M. Zingl, H. U. Strand, S.-S. B. Lee, J. von Delft, and A. Georges, Physical Review Letters **124**, 016401 (2020), ISSN 0031-9007, 1079-7114, URL <https://link.aps.org/doi/10.1103/PhysRevLett.124.016401>.

[22] I. I. Mazin and D. J. Singh, Physical Review Letters **82**, 4324 (1999), URL <https://link.aps.org/doi/10.1103/PhysRevLett.82.4324>.

[23] A. Rømer, D. Scherer, I. Eremin, P. Hirschfeld, and B. Andersen, Physical Review Letters **123**, 247001 (2019), ISSN 0031-9007, 1079-7114, URL <https://link.aps.org/doi/10.1103/PhysRevLett.123.247001>.

[24] Y. Sidis, M. Braden, P. Bourges, B. Hennion, S. NishiZaki, Y. Maeno, and Y. Mori, Physical Review Letters **83**, 3320 (1999), ISSN 0031-9007, 1079-7114, URL <https://link.aps.org/doi/10.1103/PhysRevLett.83.3320>.

[25] P. Steffens, Y. Sidis, J. Kulda, Z. Mao, Y. Maeno, I. Mazin, and M. Braden, Physical Review Letters **122**, 047004 (2019), ISSN 0031-9007, 1079-7114, URL <https://link.aps.org/doi/10.1103/PhysRevLett.122.047004>.

[26] (????), supplementary Material to this paper includes an estimation of laser heating, additional spectra at higher temperatures, in the E_g symmetry channel and at different laser wavelengths, a description of the inversion procedure of the extended Drude model, details on the Raman vertex calculations, additional study on the quadratic behavior of the scattering rate as a function of frequency and temperature, additional details on the determination of p_μ .

[27] J. S. Bobowski, N. Kikugawa, T. Miyoshi, H. Suwa, H.-s. Xu, S. Yonezawa, D. A. Sokolov, A. P. Mackenzie, and Y. Maeno, Condensed Matter **4**, 6 (2019), ISSN 2410-3896, URL <https://www.mdpi.com/2410-3896/4/1/6>.

[28] T. P. Devereaux and R. Hackl, Reviews of Modern Physics **79**, 175 (2007), URL <https://link.aps.org/doi/10.1103/RevModPhys.79.175>.

[29] S. Cobo, F. Ahn, I. Eremin, and A. Akbari, Physical Review B **94**, 224507 (2016), ISSN 2469-9950, 2469-9969, URL <https://link.aps.org/doi/10.1103/PhysRevB.94.224507>.

[30] I. P. Ipatova, A. V. Subashiev, and V. A. Voitenko, Solid State Communications **37**, 893 (1981).

[31] A. Zawadowski and M. Cardona, Physical Review B **42**, 10732 (1990), ISSN 0163-1829, 1095-3795, URL <https://link.aps.org/doi/10.1103/PhysRevB.42.10732>.

[32] C. Berthod, J. Mravlje, X. Deng, R. Žitko, D. van der Marel, and A. Georges, Physical Review B **87**, 115109 (2013), URL <https://link.aps.org/doi/10.1103/PhysRevB.87.115109>.

[33] M. Opel, R. Nemetschek, C. Hoffmann, R. Philipp, P. F. Müller, R. Hackl, I. Tüttő, A. Erb, B. Revaz, E. Walker, et al., Physical Review B **61**, 9752 (2000), ISSN 0163-1829, 1095-3795, URL <https://link.aps.org/doi/10.1103/PhysRevB.61.9752>.

[34] K. Sen, D. Fuchs, R. Heid, K. Kleindienst, K. Wolff, J. Schmalian, and M. Le Tacon, Nature Communications **11**, 4270 (2020), ISSN 2041-1723, URL <https://www.nature.com/articles/s41467-020-18092-6>.

[35] M. Udagawa, T. Minami, N. Ogita, Y. Maeno, F. Nakamura, T. Fujita, J. G. Bednorz, and F. Lichtenberg, Physica B: Condensed Matter **219-220**, 222 (1996), ISSN 09214526, URL <https://linkinghub.elsevier.com/retrieve/pii/0921452695007024>.

[36] S. Sakita, S. Nimori, Z. Q. Mao, Y. Maeno, N. Ogita, and M. Udagawa, Physical Review B **63**, 134520 (2001).

[37] M. Iliev, V. Popov, A. Litvinchuk, M. Abrashev, J. Bäckström, Y. Sun, R. Meng, and C. Chu, Physica B: Condensed Matter **358**, 138 (2005), ISSN 09214526, URL <https://linkinghub.elsevier.com/retrieve/pii/S0921452605000037>.

[38] N. E. Hussey, A. P. Mackenzie, J. R. Cooper, Y. Maeno, S. Nishizaki, and T. Fujita, Physical Review B **57**, 5505 (1998), URL <https://link.aps.org/doi/10.1103/PhysRevB.57.5505>.

[39] A. A. Husain, M. Mitrano, M. S. Rak, S. I. Rubeck, H. Yang, C. Sow, Y. Maeno, P. E. Batson, and P. Abbamonte, arXiv:2007.06670 [cond-mat] (2020), URL <https://arxiv.org/abs/2007.06670>.

[40] W. Götze and P. Wölfle, Physical Review B **6**, 1226 (1972), ISSN 0556-2805, URL <https://link.aps.org/doi/10.1103/PhysRevB.6.1226>.

doi/10.1103/PhysRevB.6.1226.

[41] G. J. McMullan, M. P. Ray, and R. J. Needs, *Physica B* **223-224**, 529 (1996).

[42] C. Veenstra, Z.-H. Zhu, M. Raichle, B. Ludbrook, A. Nicolaou, B. Slomski, G. Landolt, S. Kittaka, Y. Maeno, J. Dil, et al., *Physical Review Letters* **112**, 127002 (2014), ISSN 0031-9007, 1079-7114, URL <https://link.aps.org/doi/10.1103/PhysRevLett.112.127002>.

[43] M. J. Rice, *Physical Review Letters* **20**, 1439 (1968), ISSN 0031-9007, URL <https://link.aps.org/doi/10.1103/PhysRevLett.20.1439>.

[44] K. Kadowaki and S. B. Woods, *Solid State Communications* **58**, 507 (1986), ISSN 0038-1098, URL <http://www.sciencedirect.com/science/article/pii/0038109886907854>.

[45] N. E. Hussey, *Journal of the Physical Society of Japan* **74**, 1107 (2005), ISSN 0031-9015, 1347-4073, URL <http://arxiv.org/abs/cond-mat/0409252>.

[46] A. C. Jacko, J. O. Fjærrestad, and B. J. Powell, *Nature Physics* **5**, 422 (2009), ISSN 1745-2481, URL <https://www.nature.com/articles/nphys1249>.

[47] M. Barber, A. Gibbs, Y. Maeno, A. Mackenzie, and C. Hicks, *Physical Review Letters* **120** (2018), ISSN 0031-9007, 1079-7114.

[48] D. L. Maslov and A. V. Chubukov, *Physical Review B* **86**, 155137 (2012), ISSN 1098-0121, 1550-235X, URL <https://link.aps.org/doi/10.1103/PhysRevB.86.155137>.

[49] P. E. Sulewski, A. J. Sievers, M. B. Maple, M. S. Torikachvili, J. L. Smith, and Z. Fisk, *Physical Review B* **38**, 5338 (1988), ISSN 0163-1829, URL <https://link.aps.org/doi/10.1103/PhysRevB.38.5338>.

[50] U. Nagel, T. Uleksin, T. Rööm, R. P. S. M. Lobo, P. Lejay, C. C. Homes, J. S. Hall, A. W. Kinross, S. K. Purdy, T. Munsie, et al., *Proceedings of the National Academy of Sciences of the United States of America* **109**, 19161 (2012), ISSN 0027-8424, URL <https://www.ncbi.nlm.nih.gov/pmc/articles/PMC3511099/>.

[51] S. I. Mirzaei, D. Stricker, J. N. Hancock, C. Berthod, A. Georges, E. v. Heumen, M. K. Chan, X. Zhao, Y. Li, M. Greven, et al., *Proceedings of the National Academy of Sciences* **110**, 5774 (2013), ISSN 0027-8424, 1091-6490, URL <https://www.pnas.org/content/110/15/5774>.

[52] A. Tytarenko, Y. Huang, A. de Visser, S. Johnston, and E. van Heumen, *Scientific Reports* **5**, 12421 (2015), ISSN 2045-2322, URL <https://www.nature.com/articles/srep12421>.

[53] A. Pustogow, Y. Saito, A. Löhle, M. S. Alonso, A. Kawamoto, V. Dobrosavljević, M. Dressel, and S. Fratini, arXiv:2101.07201 [cond-mat] (2021), URL <http://arxiv.org/abs/2101.07201>.

[54] O. Gingras, R. Nourafkan, A.-M. S. Tremblay, and M. Côté, *Physical Review Letters* **123**, 217005 (2019), ISSN 0031-9007, 1079-7114, URL <https://link.aps.org/doi/10.1103/PhysRevLett.123.217005>.

[55] H. G. Suh, H. Menke, P. M. R. Brydon, C. Timm, A. Ramires, and D. F. Agterberg, *Phys. Rev. Research* **2**, 032023 (2020), URL <https://link.aps.org/doi/10.1103/PhysRevResearch.2.032023>.

[56] I. I. Mazin and D. J. Singh, *Physical Review Letters* **79**, 733 (1997), ISSN 0031-9007, 1079-7114, URL <https://link.aps.org/doi/10.1103/PhysRevLett.79.733>.

[57] P. B. Allen, *Physical Review B* **92**, 054305 (2015).

[58] J. K. Freericks, T. P. Devereaux, and R. Bulla, *Physical Review B* **64**, 233114 (2001).

[59] N. Li, E. Gull, and A. J. Millis, *Physical Review Letters* **109**, 106401 (2012).

Supplementary Material to "Orbital dichotomy of Fermi liquid properties in Sr_2RuO_4 revealed by Raman spectroscopy"

Evaluation of the laser heating

To assess the actual laser spot temperature on the sample, we consider firstly T_m the temperature measured by a silicon diode sensor in contact with the sample through the copper sample holder (the sample is fixed on the sample holder via thermally-conductive silver paint) and secondly the local heating due to the laser, which depends on the beam power P . To evaluate this heating, we compare spectra taken at the same $T_m = 10$ K for different P (2, 4 and 6 mW), and spectra taken at the same $P = 2$ mW for different T_m between 9 and 17 K. We compare intensity spectra, and not Raman response spectra, because in the latter case we have to assume the temperature of the sample to derive the Bose factor.

We find that increasing P by 2 mW has the same effect on the spectra than increasing T_m by 4 K (fig. S1). So we conclude that we must consider a laser heating of 4 ± 1 K for the spectra we obtained at 2 mW. We assume that in the temperature range considered for the core of the analysis (T_m from 3 to 40 K), the laser heating stays constant within ± 1 K uncertainty.

Spectra in E_g symmetry

The Fig. S2 shows the experimental Raman response in the E_g channel. In E_g as in A_{1g} (compared to the in-plane symmetries), the Drude peaks are melted into the FL foot even at the lowest temperatures, indicating larger relaxation rates. The small narrow peak developing under 20 K centered around 3.5 meV in A_{1g} could be also present in E_g . To the best of our knowledge, the narrow E_g mode centered around 16.5 meV had not been observed yet and could correspond to the second predicted Raman allowed phonon E_g mode [35].

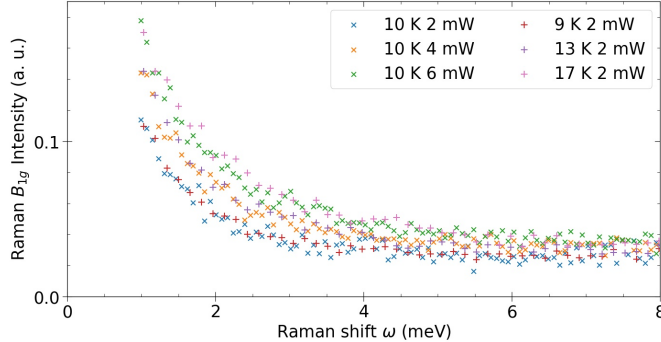


FIG. S1: Evaluation of the laser heating. The spectra have been renormalized with respect to each other by a multiplicative constant, in order to compare spectra taken at different laser beam powers.

Spectra at higher temperatures

The Fig. S3 shows the experimental Raman spectra in the B_{1g} and B_{2g} symmetry channels at selected temperatures, mostly above 50 K. We observe the disappearance of the FL dip between 85 and 105 K in B_{1g} . In B_{2g} the clear disappearance of the FL dip is harder to resolve, but occurs below 40-50 K.

We note in the main text that the disappearance of the FL dip occurs theoretically when $\Gamma_{\mu,0} \sim \frac{1}{\alpha_\mu}$. However at the temperatures where we experimentally observe this disappearance, we can not properly define α_μ , so the examination of this condition is difficult. Also a quantitative examination is prevented by the choice of ω_c (see section), which impacts the quantitative values of $\Gamma_{\mu,0}$ and $\frac{1}{\alpha_\mu}$. These restrictions being considered, we try nevertheless to look at which temperature T_d we have $\Gamma_{\mu,0} \sim \frac{1}{\alpha_\mu}$, by taking the constant values of α_μ obtained in the FL regime (see fig S5 for the high temperature values of $\Gamma_{\mu,0}$). We obtain $T_{d,B_{1g}} \approx 120\text{-}150$ K and $T_{d,B_{2g}} \approx 30\text{-}50$ K, so a rather good agreement with the expectation in B_{2g} and a small overestimation in B_{1g} .

Extraction of the Fermi liquid parameters

To perform the analysis of the FL parameters, we extract them from the Raman spectra by following the memory-function approach, first introduced in the optical conductivity data, and introduced by Opel et al. [33] for the Raman response analysis. We only present here the practical implementation of this approach. In this section we drop the symmetry μ index and the

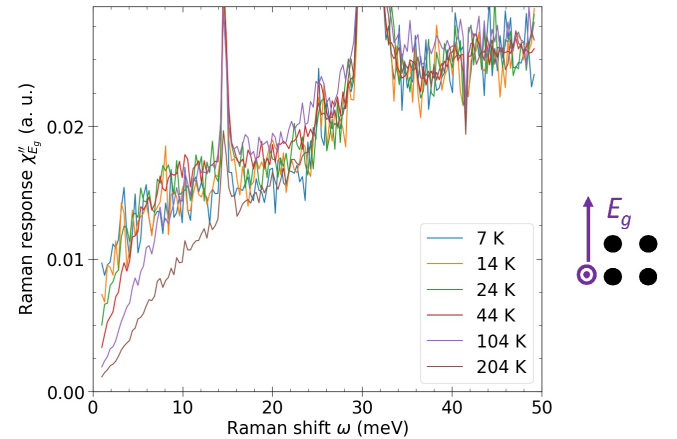


FIG. S2: Experimental Raman response obtained in the E_g symmetry at selected temperatures. The sketch on the right depicts the polarizations of the incident and scattered beams with respect to the in-plane Ru square lattice.

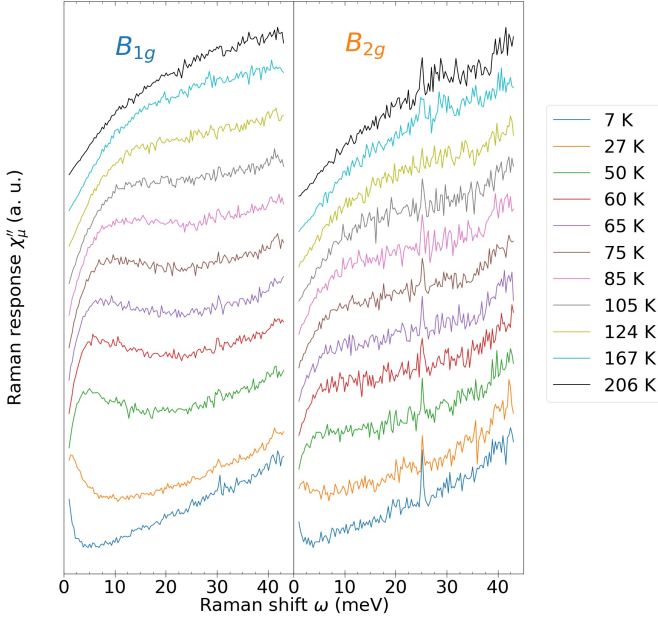


FIG. S3: Behavior of the experimental B_{1g} and B_{2g} Raman spectra above 50 K. The spectra are shifted along the ordinate axis for better clarity.

temperature dependence.

In the extended Drude model hypothesis the electronic Raman response is expressed as :

$$\chi''(\omega) = \frac{\chi^0}{1 + \lambda(\omega)} \frac{\omega \tilde{\Gamma}(\omega)}{\omega^2 + \tilde{\Gamma}(\omega)^2} \quad (\text{S5})$$

with $\tilde{\Gamma}_\mu(\omega) = \frac{\Gamma_\mu(\omega)}{1 + \lambda_\mu}$, Γ the Raman relaxation rate and $1 + \lambda = \frac{m^*}{m_b}$ the Raman mass-enhancement factor (with respect to the band mass). χ^0 is the static susceptibility. We compute two auxiliary functions I and K . I stands for the Raman conductivity and ωK is the Kramers-Krönig transform of I .

$$I(\omega) = \frac{\chi''(\omega)}{\omega} \quad (\text{S6})$$

$$K(\omega) = -\frac{2}{\pi} \mathcal{P} \int_0^{\omega_c} d\xi \frac{I(\xi)}{\xi^2 - \omega^2} \quad (\text{S7})$$

The \mathcal{P} symbol represents the principal value. We compute the static susceptibility χ^0 which will act here as a renormalization factor :

$$\chi^0 = \frac{2}{\pi} \int_0^{\omega_c} d\omega I(\omega) \quad (\text{S8})$$

Then Γ and $1 + \lambda$ are expressed as

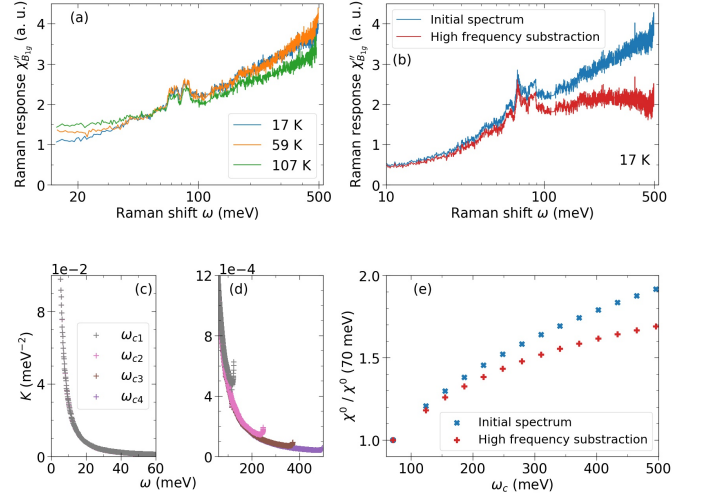


FIG. S4: (a) Experimental Raman response obtained in the B_{1g} symmetry channel at selected temperatures with the single-grating spectrometer (b) High energy linear increase subtraction on the 17 K spectrum. Here the spectrum before subtraction consists of the concatenation of the spectra taken on the triple-mode spectrometer (below 70 meV) and on the simple-mode spectrometer (above 70 meV), properly renormalizing one with respect to the other. A linear signal is subtracted on the whole response to obtain the high energy subtracted response. (c,d) Influence of ω_c on K for the B_{1g} -17 K spectrum. In the (c) panel, all the data overlap. (e) Influence of ω_c on χ^0 for the B_{1g} -17 K spectrum. The χ^0 values are normalized with respect to its value for $\omega_c = 70$ meV.

$$\Gamma(\omega) = \chi^0 \frac{I(\omega)}{[I(\omega)]^2 + [\omega K(\omega)]^2} \quad (\text{S9})$$

$$1 + \lambda(\omega) = \chi^0 \frac{K(\omega)}{[I(\omega)]^2 + [\omega K(\omega)]^2} \quad (\text{S10})$$

To calculate the integrals in the expressions of K and χ^0 , we have to know the electronic Raman response down to 0 meV. As our experimental low energy cut-off (due to the elastic scattering of light on the sample) is 1 meV, we extrapolate the Raman response to zero energy using a simple Drude model fitting the data below 2.5 meV. For the spectra below 12 K, these fits have a rather high margin of error, as the maximum of the Drude peak falls below the experimental cut-off. This explains the large dispersion of the extracted FL parameters below 12 K, with respect to the ones above 12 K.

In the expressions of K and χ^0 appears a cut-off energy ω_c whose choice we discuss now. From the theoretical form of the Raman response in the extended Drude model (equation (2)), if we consider a FL behavior up to infinite energy, then χ'' decreases to 0 as $1/\omega$. So both integrals used for deriving K and χ^0 converge for $\omega_c \rightarrow \infty$. We could conclude that by

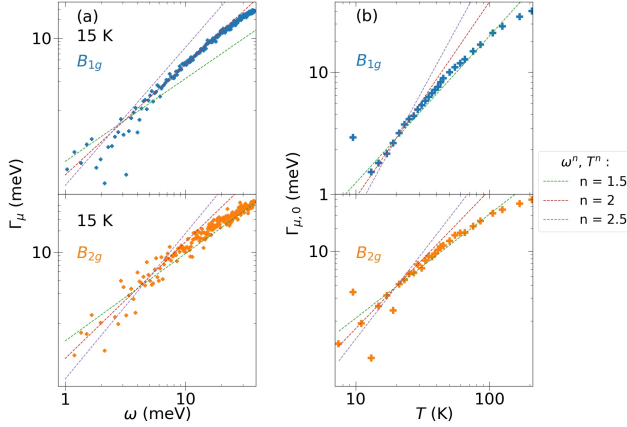


FIG. S5: Energy ((a) panel) and temperature ((b) panel) dependencies of $\Gamma_{B_{1g}}/B_{2g}$, plotted in log-log scale. The green plus symbol points are the extracted experimental parameters and the dashed lines are guides to the eye for three different exponents behaviors.

taking ω_c as high as experimentally possible, we would approach the genuine values of K and χ^0 . However we expect interband transitions to start contributing at higher energy potentially spoiling our analysis, which assumes only intraband excitations. Without a precise knowledge of the spectral lineshape of these transitions, a correct interpolation of the spectra at high energy is not straightforward and the choice of the optimal energy cutoff is therefore not trivial. With these caveats in mind, we acquired additional high energy Raman spectra, up to 0.5 eV, in the B_{1g} symmetry and studied the influence of the choice of ω_c on K and χ^0 (Fig. S4).

At all temperatures, the experimental spectra display a quasi-linear increase between 125 and 500 meV. Taking $\Gamma(\omega) \sim \omega^n$ at high energy, χ'' goes as a constant for $n = 1$, decreases for $n > 1$ and increases for $n < 1$. $n < 1$ seems unphysical and we rather expect a decrease of n from 2 to 1. So the origin of the increase of the Raman response cannot be understood in terms of the extended Drude model Raman response. We attribute it to the onset of interband transitions, but we cannot rule out a luminescence origin. Subtracting the linear increase, we obtain Raman response spectra which go roughly as a constant above 125 meV. As long as we restrict the analysis in the range $\omega \leq \frac{\omega_c}{2}$, the choice of ω_c does not strongly affect K . On the other hand, χ^0 depends strongly on ω_c , with a logarithmic increase with ω_c . $\Gamma(\omega)$ and $1 + \lambda(\omega)$ are directly proportional to χ^0 , so it is the case also for Γ_{00} , α , β and $1 + \lambda(\omega \rightarrow 0)$. This logarithmic increase of χ^0 with ω_c induces for the values of the various FL parameters a dependence on the choice of ω_c . For this reason we believe the extracted FL parameters using $\omega_c = 71$ meV are likely underestimated.

Still, since in our work we mainly focus on a

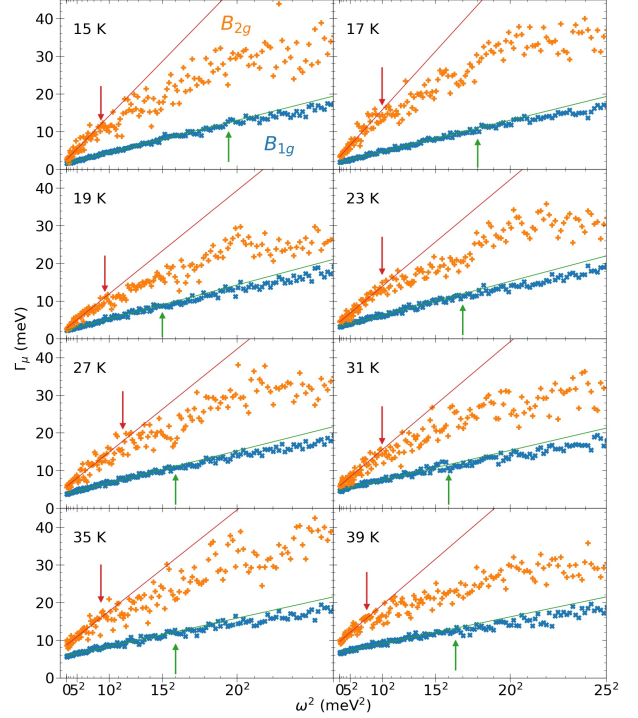


FIG. S6: Energy dependencies of $\Gamma_{B_{1g}}/B_{2g}$, plotted in quadratic scale at different temperatures between 15 and 40 K. The solid lines are quadratic fits to the lowest-energy data. The arrows point to the energies above which the deviation from the quadratic behavior becomes visually flagrant.

qualitative comparative study between the B_{1g} and B_{2g} FL parameters, an optimal choice of ω_c is not paramount, as long as it is the same for the analysis in both symmetries. For the results presented in this paper, we choose $\omega_c = 71$ meV (the upper limit of our energy range) and restrict ourselves to $\omega \leq 31$ meV for the analysis.

Quadratic behavior of the relaxation rate and Gurzhi scaling

In the main text (fig. 3 and 4), we show the quadratic behavior of Γ_μ in both energy and temperature, by using a quadratic x-axis. In fig S5, we plot $\Gamma_\mu(\omega, T = 15$ K) and $\Gamma_{\mu,0}$ in logarithmic scales to clarify the quadratic behaviors. At 15 K in B_{1g} , the ω^2 behavior appears very clearly up to 20 meV, whereas in B_{2g} it is less robust, with a clear deviation above 8-9 meV towards $\omega^{1.5}$, even if the ω^2 behavior seems the more appropriate at low energy with respect to $\omega^{1.5}$ and $\omega^{2.5}$. Concerning the temperature behavior, disregarding the lowest temperatures in B_{1g} (below 12 K) and the most scattered points in B_{2g} , the T^2 behavior appears clearly up to 30 K in both symmetries.

To further evaluate $\omega_{FL,\mu}$, and its possible temperature dependence, we study the energy quadratic

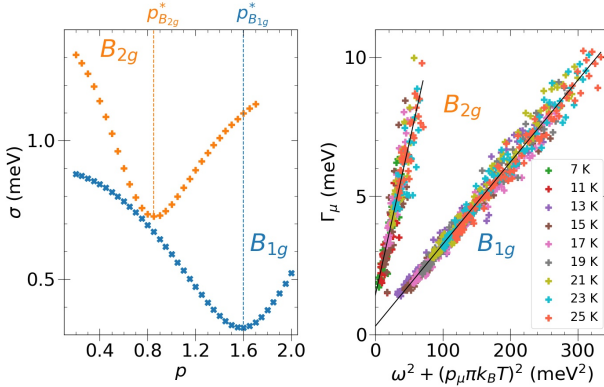


FIG. S7: Determination of the best value of p_μ verifying the Gurzhi scaling law. On the right panel, the black lines are linear fits to the experimental data (plus symbol points).

behavior of Γ_μ for different temperatures between 15 and 40 K (fig. S6). The solid lines are quadratic fits to the lowest-energy data (below 15 and 8 meV respectively for B_{1g} and B_{2g}) and the arrows point to the energies above which the deviation from the quadratic behavior becomes visually flagrant. In B_{1g} at all temperatures, the deviation is clear above 20 meV. There is also a clear trend towards deviations at lower energies when raising the temperature, consistent with a weakening of the FL state: for $T > 30$ K, deviations are visible already at ~ 16 meV. In B_{2g} it is less simple to conclude but depending on temperatures the deviation is visible above 8-12 meV. So due to the uncertainties of our measurements, we only conclude that $\omega_{FL,B_{1g}} \in [15,20]$ meV and $\omega_{FL,B_{2g}} \in [8,12]$ meV, with a clear quantitative dichotomy between the two channels.

The Gurzhi scaling is showed in fig. 4 of the main text. To determine the values p_μ^* of p_μ that correspond optimally to the scaling, we adopt a method illustrated in fig S7. At fixed symmetry, for values of p_μ in a range between 0.2 and 2, we compute $\omega^2 + (p_\mu \pi k_B T)^2$ for a set of selected temperatures between 10 K and 30 K. Then we fit $\Gamma_\mu(\omega, T)$ linearly with respect to $\omega^2 + (p_\mu \pi k_B T)^2$, and we obtain the standard deviation σ of the fit. By plotting σ with respect to p_μ , we obtain p_μ^* as the value

of p_μ which minimizes σ , namely 1.6 (± 0.1) and 0.85 (± 0.1) respectively for B_{1g} and B_{2g} .

Raman vertex calculation

To interpret the experimental FL dichotomy between the two Raman channels B_{1g} and B_{2g} , we compute the Raman vertices $\gamma^\mu(\mathbf{k})$ using a 3 orbital tight-binding model. We take the orbital transition energies $\epsilon_{m,n}(\mathbf{k})$ between Ru 4d orbitals m and n as (with $\epsilon_m = \epsilon_{m,m}$):

$$\epsilon_{xz}(\mathbf{k}) = -2t_1 \cos(k_x) - 2t_2 \cos(k_y) \quad (S11)$$

$$\epsilon_{yz}(\mathbf{k}) = -2t_2 \cos(k_x) - 2t_1 \cos(k_y) \quad (S12)$$

$$\epsilon_{xy}(\mathbf{k}) = -2t_3(\cos(k_x) + \cos(k_y)) - 4t_4 \cos(k_x) \cos(k_y) \quad (S13)$$

$$\epsilon_{xz,yz}(\mathbf{k}) = \epsilon_{xz,yz}(\mathbf{k}) = -4t_5 \sin(k_x) \sin(k_y) \quad (S14)$$

$$\epsilon_{xz,xy}(\mathbf{k}) = \epsilon_{yz,xy}(\mathbf{k}) = 0 \quad (S15)$$

(see also the figure 1 in the main text for the definition of the hopping integrals t_i). In the effective mass approximation, the Raman vertices in B_{1g} and B_{2g} are obtained through:

$$\gamma_{mn}^{B_{1g}}(\mathbf{k}) = \frac{1}{2} \left(\frac{\partial^2 \epsilon_{mn}(\mathbf{k})}{\partial k_x^2} - \frac{\partial^2 \epsilon_{mn}(\mathbf{k})}{\partial k_y^2} \right) \quad (S16)$$

$$\gamma_{mn}^{B_{2g}}(\mathbf{k}) = \frac{\partial^2 \epsilon_{mn}(\mathbf{k})}{\partial k_x \partial k_y} \quad (S17)$$

So in the orbital basis (d_{xz}, d_{yz}, d_{xy}) , $\gamma_{orb}^{B_{1g}}(\mathbf{k})$ and $\gamma_{orb}^{B_{2g}}(\mathbf{k})$ read as:

$$\gamma_{orb}^{B_{1g}}(\mathbf{k}) = \begin{pmatrix} t_1 \cos(k_x) - t_2 \cos(k_y) & 0 & 0 \\ 0 & t_2 \cos(k_x) - t_1 \cos(k_y) & 0 \\ 0 & 0 & t_3(\cos(k_x) - \cos(k_y)) \end{pmatrix} \quad (S18)$$

$$\gamma_{orb}^{B_{2g}}(\mathbf{k}) = \begin{pmatrix} 0 & -4t_5 \cos(k_x) \cos(k_y) & 0 \\ -4t_5 \cos(k_x) \cos(k_y) & 0 & 0 \\ 0 & 0 & -4t_4 \sin(k_x) \sin(k_y) \end{pmatrix} \quad (S19)$$

The Raman response in each intra or interorbital

transition component is proportional to the square of

the corresponding Raman vertex $\gamma_{n,m}^\mu$, so to t_i^2 . Note that the inter-orbital hopping integral t_5 is at least one order of magnitude smaller than t_1 , t_3 and t_4 [56], so that the non-diagonal inter-orbital processes will make negligible contribution to the B_{2g} Raman response. With the values of t_i taken in the main text, and ignoring inter-orbital processes, we expect $\chi''_{B_{1g}} \geq \chi''_{B_{2g}}$ which is consistent with the experiments where the B_{1g} Raman response is significantly stronger than the B_{2g} one.

We note that the effective mass approximation is justified if only non-resonant Raman process are considered. The relevance of resonant Raman processes can be assessed by looking at the dependence of the Raman spectra on the incoming laser wavelength. To check this, we obtained B_{1g} and B_{2g} Raman spectra with two other incident laser wavelengths, namely 488 and 660 nm. As shown in table S2, the intensity ratio between the two symmetries stays similar in the three wavelengths, indicating no significant resonant behavior, and further validating the use of the effective mass approximation.

FL parameters at 660 nm

In this section, we present the spectra we obtained in B_{1g} with a 660 nm laser and the extracted FL parameters, comparing the results and analysis with the 532 nm-case. For the analysis presented in this section, we took the same $\omega_c = 41$ meV for both laser wavelength, so the reported FL values for 532 nm are quantitatively different here from the ones presented elsewhere in this paper.

Figure S8-(a) shows the temperature dependence of the low energy Raman response with a 660 nm incident laser. We observe the same spectra shape than in the 532 nm case, with spectra featuring both a Drude peak and a FL dip. The Drude peak goes to higher energy as temperature increases, and the FL dip gets resorbed. Figure S8-(b), (c) and (d) show the temperature dependence of respectively $\alpha_{B_{1g}}$, $\Gamma_{B_{1g},0}$ and $1 + \lambda_{B_{1g}}(\omega \rightarrow 0)$, comparing the 532 and 660 nm cases. We observe no significant qualitative difference in the extracted FL parameters between the two incident wavelengths, with good quantitative resemblance in particular in $\alpha_{B_{1g}}$ and $\Gamma_{B_{1g},0}$ in the FL regime below 30 K. We believe this further justifies the use of the effective mass approximation.

| | B_{1g}/B_{2g} χ'' ratio |
|--------|--------------------------------|
| 488 nm | 2.8 |
| 532 nm | 3.7 |
| 660 nm | 3.4 |

TABLE S2: $B_{1g}-B_{2g}$ Raman response ratio for three incident laser wavelengths. We define the ratio as the average of the spectra ratio between 12 and 36 meV.

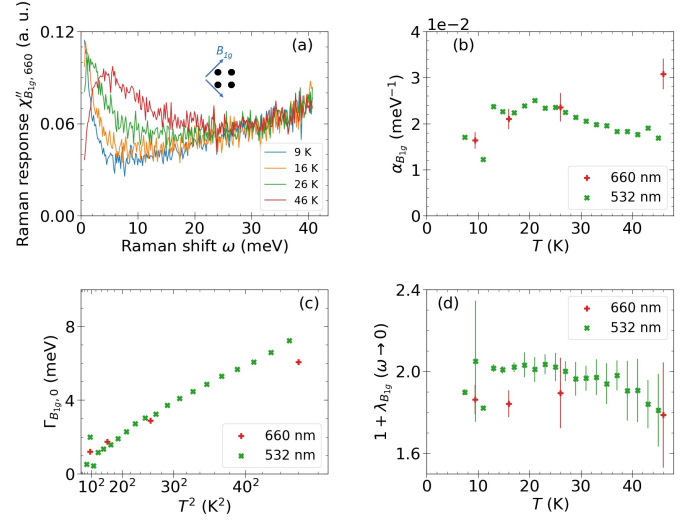


FIG. S8: FL behavior probed in B_{1g} symmetry with a 660 nm incident laser. (a) Raman response at selected temperatures. The sketch depicts the polarizations of the incident and scattered beams with respect to the in-plane Ru square lattice. (b) Temperature dependence of the ω^2 prefactor $\alpha_{B_{1g}}$ at both 532 and 660 nm. (c) Temperature dependence of the static relaxation rate $\Gamma_{B_{1g},0}$ at both 532 and 660 nm. (d) Temperature dependence of the low-energy mass renormalization factor $1 + \lambda_{B_{1g}}(\omega \rightarrow 0)$ at both 532 and 660 nm.

Link between one particle FL parameters and the extended Drude model

Neglecting vertex corrections, the Raman response can be written in terms of the single particle spectral functions A [28]:

$$\chi'' = \frac{2}{\pi} \sum_k \gamma_k^2 \int_{-\infty}^{\infty} d\epsilon [f(\epsilon) - f(\epsilon + \omega)] A(k, \epsilon) A(k, \epsilon + \omega) \quad (S20)$$

γ_k is the Raman vertex whose k dependence will depend on the symmetry and f is the Fermi-Dirac distribution function $f = \frac{1}{e^{\frac{\epsilon}{k_B T}} + 1}$. The spectral functions can be written in terms of the complex one electron self-energy $\Sigma = \Sigma_1 + i\Sigma_2$:

$$A(k, \epsilon) = \frac{1}{\pi} \frac{\Sigma_2(k, \epsilon)}{(\epsilon - \epsilon_k - \Sigma_1(k, \epsilon))^2 + \Sigma_2^2(k, \epsilon)} \quad (S21)$$

where ϵ_k is the electronic dispersion. Σ_1 renormalize the electron dispersion and is related to the mass enhancement and Σ_2 is the inverse of the electron lifetime, which is now a quasiparticle.

The expressions for Σ depend on the nature of electron interactions: electron-impurity, electron-phonon, electron-electron. For a FL we assume that the dominant interaction are electron-electron interactions. In that case we have the following form for of the electron self-energy at low energy (below the FL energy scale ω_{FL} [32]):

$$\Sigma(\epsilon, T) = (1 - \frac{1}{Z})\epsilon - \frac{i}{Z\pi k_B T_0}(\epsilon^2 + \pi^2 k_B^2 T^2) \quad (\text{S22})$$

where Z is the quasiparticle residue which is also the inverse of the mass enhancement $Z = \frac{m}{m^*}$, $k_B T_0$ is an energy scale of electronic interactions which is typically much greater than ω_{FL} [32].

For isotropic impurity scattering the self-energy is just an imaginary constant $\Sigma = -i\Sigma_2(0)$ where $\Sigma_2(0)$ is the single particle scattering rate. In that case an analytical Drude-like form for the Raman response can be given [30]:

$$\chi'' = \chi_\gamma^0 \frac{2\omega\Sigma_2(0)}{\omega^2 + (2\Sigma_2(0))^2} = \chi_\gamma^0 \frac{\omega\Gamma_0}{\omega^2 + \Gamma_0^2} \quad (\text{S23})$$

where χ_γ^0 contains an Fermi surface average of the square of the Raman vertex γ_k . Here we see that the Raman two-particle scattering rate Γ_0 is twice the single particle scattering $\Sigma_2(0)$. For a k dependent static scattering a similar formula is given by Zawadowski and Cardona [31] where Γ_0 is replaced by a symmetry dependent effective scattering rate Γ_0^L and L is the symmetry of the Raman vertex.

As for conductivity, for a general energy and k dependent self-energy, no analytical form of the Raman response can be given. In general we must use a more phenomenological approach in terms of memory function [40] or, equivalently, an extended (or generalized) Drude formula. Starting from the memory function approach of a response function:

$$\chi(\omega) = \chi_0 \frac{M(\omega)}{\omega + M(\omega)} \quad (\text{S24})$$

where $M(\omega)$ is a complex memory function $M = M' + iM''$ (here we drop the Raman vertex γ which is implicit from now on). M'/M'' are odd/even functions of ω and are related by Kramers-Kronig relations to satisfy causality [40]. The imaginary part of the response function is:

$$\chi''(\omega) = \chi_0 \frac{\omega M'(\omega)}{(\omega + M'(\omega))^2 + M''^2(\omega)} \quad (\text{S25})$$

To obtain the extended Drude formula we make the following identification with the energy dependent scattering rate $\Gamma(\omega)$ and the mass enhancement $1+\lambda(\omega)$: $M''(\omega) = \Gamma(\omega)$ and $\omega\lambda(\omega) = M'(\omega)$.

$$\chi''(\omega) = \frac{\chi_0}{1+\lambda} \frac{\omega\tilde{\Gamma}(\omega)}{\omega^2 + \tilde{\Gamma}^2(\omega)} \quad (\text{S26})$$

$$\text{where } \tilde{\Gamma}(\omega) = \frac{\Gamma(\omega)}{1+\lambda}$$

While this is formally correct for any response function, the link between the two-particle and one particle mass enhancement and scattering rates is not straightforward anymore. Still, as argued by Berthod et al. and

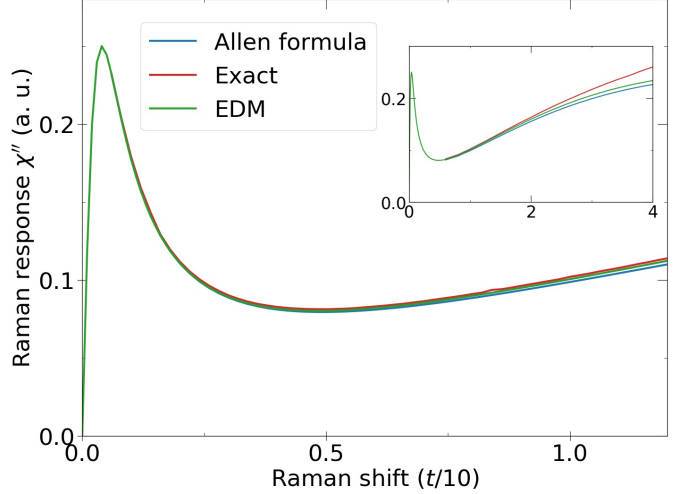


FIG. S9: Comparison between the exact expression of the Raman response (ignoring vertex corrections), the Allen formula S27 and the extended Drude model. For the exact response a standard 2D tight-binding electronic structure $\epsilon_k = -2t(\cos(k_x a) + \cos(k_y a)) - 4t' \cos(k_x a) \cos(k_y a) - \mu$ (with $t'/t=0.5$) and a $\cos(k_x a) - \cos(k_y a)$ B_{1g} -like vertex were taken. The single particle FL parameters were $Z = 1/2$, $g_0 = 0.004t$ and $\alpha = \frac{50}{t}$ for both the exact response and the approximation S27. For the extended Drude model the parameters were $1 + \lambda = 1/Z = 2$, $\Gamma_0 = 2g_0$ and $\alpha_{Drude} = 2/3\alpha$. Inset: spectra at higher energies showing significant deviations between the exact response and both the Allen formula and extended Drude model.

Allen [32, 57], in the case of weak k dependence an approximate relationship between both quantities can be given provided we ignore vertex corrections. Vertex corrections vanish for the optical conductivity if the self energy has no k dependence. A similar conclusion can be reached for non-resonant Raman scattering [58].

To assess the link between the single particle FL parameters of the exact response and the 2-particle FL parameter of the extended Drude model, we compare both responses using generic FL parameters. The single particle self energy can be written as $\Sigma(\epsilon, T) = (1 - \frac{1}{Z})\epsilon - i(g_0 + \alpha\epsilon^2)$ where g_0 is the static single particle scattering rate. For simplicity we will take a single band 2D tight binding model on a square lattice for the dispersion: $\epsilon_k = -2t(\cos(k_x a) + \cos(k_y a)) - 4t' \cos(k_x a) \cos(k_y a) - \mu$ where t and t' are nearest and next-nearest neighbour hoppings, and a is the lattice parameter.

In figure S9, we compare the response computed using the exact formula with the spectrum obtained using the extended Drude formula with a scattering rate $\Gamma = \Gamma_0 + \alpha_{Drude}\omega^2$ and $1 + \lambda = \frac{1}{Z}$. Also shown is the spectrum obtained using an approximation for the Raman response valid for local FL derived by Berthod et al. and Allen [32, 57] in the case of optical conductivity (hereafter named "Allen formula"):

$$\chi''_\gamma = \frac{2}{\pi} \Gamma_\gamma(0) \int_{-\infty}^{\infty} d\epsilon [f(\epsilon) - f(\epsilon + \omega)] \times \Re \left(\frac{i}{\omega + \Sigma^*(\epsilon) - \Sigma(\epsilon + \omega)} \right) \quad (\text{S27})$$

Taking Γ_0 and α_{Drude} as free parameters (Z is kept identical), a good agreement is found at low energy using $\Gamma_0 = 2g_0$ and $\alpha_{Drude} = 2/3\alpha$. Using these parameters for the single particle and two-particle FL parameters, all three responses agree in the region of the Drude peak and the FL "dip". Deviations start at energies of the order of the band width t , which we attribute to changes in the electron density of states due to the non-parabolicity of the band structure.

In general deviation from this relationship will be seen for strongly k dependent self-energies where the FL parameter will acquire a symmetry dependence even for a single band. Vertex corrections will also modify differently the one particle and two-particle properties whenever a strong k dependence exists. Cluster extensions of DMFT have been used to evaluate vertex corrections for the Raman response of the single band Hubbard model on a square lattice by Lin et al. [59]. The impact of vertex corrections was found to be strong close to the Mott transition and at high energies where they are essential to reproduce the two-magnon peak. Their impact weaken at low energy when moving away from the Mott regime. To our knowledge similar calculations for multiband systems are not available.

For a multiband system like Sr_2RuO_4 , assuming that the self-energy are orbital but not k dependent and with small inter-orbital coupling, the above approximation will be correct for each individual orbital. The total Raman response will be a sum of each orbital-derived band contributions, with weight given by the k -integrated Raman vertices along each band. A potential source of complication in Sr_2RuO_4 is the spin-orbit coupling which mixes the orbital content of each band along the Brillouin zone diagonal.